

OPEN

Study of biopolymer encapsulated Eu doped Fe_3O_4 nanoparticles for magnetic hyperthermia application

Krishna Priya Hazarika & J. P. Borah[✉]

An exciting prospect in the field of magnetic fluid hyperthermia (MFH) has been the integration of noble rare earth elements (Eu) with biopolymers (chitosan/dextran) that have optimum structures to tune specific effects on magnetic nanoparticles (NPs). However, the heating efficiency of MNPs is primarily influenced by their magnetization, size distribution, magnetic anisotropy, dipolar interaction, amplitude, and frequency of the applied field, the MNPs with high heating efficiency are still challenging. In this study, a comprehensive experimental analysis has been conducted on single-domain magnetic nanoparticles (SDMNPs) for evaluating effective anisotropy, assessing the impact of particle-intrinsic factors and experimental conditions on self-heating efficiency in both noninteracting and interacting systems, with a particular focus on the dipolar interaction effect. The study successfully reconciles conflicting findings on the interaction effects in the agglomeration and less agglomerated arrangements for MFH applications. The results suggest that effective control of dipolar interactions can be achieved by encapsulating Chitosan/Dextran in the synthesized MNPs. The lower dipolar interactions successfully tune the self-heating efficiency and hold promise as potential candidates for MFH applications.

Keywords Magnetic hyperthermia, Dipolar interactions, Magnetic anisotropy, Saturation magnetization, Biopolymers

In light of the emerging biomedical applications enabled by magnetic nanoparticles (MNPs), such as bioimaging, drug delivery, biosensors, and magnetic fluid hyperthermia (MFH), understanding and managing particle-intrinsic characteristics, colloidal parameters, and spatial coordination play a crucial role in determining the MNPs magnetic relaxation behavior¹. As a result, these parameters significantly influence MFH as a cancer cure, as they determine the energy losses converted into heat from colloidal magnetic nanoparticles under a high-frequency AC magnetic field². Presently, the optimization of magnetic nanoparticle (MNP) heating efficiency is centered around designing MNPs with tailored properties, such as specific size, effective magnetic anisotropy (K_{eff}), or saturation magnetization (M_s). Nevertheless, the challenge of simultaneously optimizing all characteristics under diverse experimental characteristics for magnetic hyperthermia remains unresolved. Recent studies have demonstrated that interparticle interactions have notable effects on the relaxation time, blocking temperature, and the hysteresis loops or specific absorption rate (SAR), with additional analyses focused on heat dissipation within agglomerated systems³. Despite numerous studies and diverse approaches on the topic, the impact of dipolar interactions on the SAR of suitably designed MNP systems remains a subject of ongoing controversy. Among the MNPs, spinel ferrite Fe_3O_4 has encountered much insight into biomedical applications due to its high biocompatibility and suitable magnetic properties^{1,2}. Therefore, the advancement of nanomaterials, and one notable example is stabilizing the Fe_3O_4 (FO) nanoparticles via different dopants in the FO matrix. Following the literature, RE ions doped in an octahedral site of the Fe_3O_4 system can stabilize and reduce the conversion possibility to maghemite or hematite^{3,4}. Additionally, Eu-doped spinel ferrite MNPs draw significant attention, due to their biocompatibility and their unique magnetic and optical properties¹. In literature, engineered Eu-doped nanoparticles provoke interest in multimodal therapeutic applications owing to their enhanced magnetic resonance imaging (MRI) properties and the nature of biocompatibility^{1,2}. Furthermore, because of the analogous ionic radii of Fe and Eu, the lesser doping concentration would not lead to the variation of the structural configuration, which

Nanomagnetism Group, Department of Physics, National Institute of Technology Nagaland, Dimapur, Nagaland 797103, India. [✉]email: jpborah@rediffmail.com

pays a great deal of prominence to the researchers. This study aims to extend our research on the Eu doping of Fe_3O_4 MNPs by introducing a coating agent (chitosan/dextran) and investigating the role of dipolar interactions and effective magnetic anisotropy in enhancing heating performance⁴. In the previous research, Eu-doped Fe_3O_4 (EuFO) matrix with different concentrations has been studied, with a primary focus on investigating the role of site-preferred substitution to tune magnetic and structural parameters to improve the self-heating efficiency for MFH applications. In this context, 7% Eu doped FO MNPs show an optimum result for MFH applications, and the study highlights that the dispersion of MNPs in aqueous solutions poses an additional challenge, primarily due to their mutual magnetic interactions and high surface energies, leading to the tendency of MNPs to agglomerate. The clustered MNPs often promote MNPs-density inhomogeneities, producing non-homogenous heating in the synthesized samples. To counter this consequence on MFH performance, the present consensus is that the engineered MNPs should possess controlled aggregation to consider the dominant contribution of dipolar interactions to correctly determine the magnetic characteristic parameters. Furthermore, based on the existing literature, the widely adopted approach to control aggregation is the effective conjugation of biomolecules such as peptides, oligonucleotides, antibodies, and natural polymers^{1,7–11}. According to previous studies, chitosan and dextran have emerged as highly promising candidates for encapsulating engineered RE-doped FO MNPs due to their non-antigenic, biocompatible, bio-functional, and biodegradable nature^{10–19}. In this work, a novel experimental approach is presented to accurately understand the role of dipolar interactions and heating efficiency, with the specific goal of distinguishing energy contributions towards MFH applications.

Experimental sections

Synthesis of the MNPs

The synthesizing technique for EuFO MNPs is explained thoroughly in the prior work⁴. The synthesis of Eu-doped Fe_3O_4 MNPs coated with chitosan and dextran has followed the identical procedure outlined in the prior study¹⁸. Henceforth, only pen the brief expression of the synthesizing route for chitosan and dextran-coated Eu-doped Fe_3O_4 MNPs and it is comprehended in Fig. 1.

All the reference MNPs were synthesized using the co-precipitation method, and the resulting EuFO was additionally surface-modified with biopolymers, specifically chitosan and dextran, referred to as CEuFO and DEuFO in this article. In the experimental protocol, 0.25 g of chitosan was dispersed in 100 ml of a 0.1 M acetic acid solution, and this mixture was slowly added drop by drop to 0.5 g of EuFO suspended in 10 ml of milli-Q water. The stirring was maintained at 180 rpm for 20 min, followed by a 15-min ultrasonication period. Following this, the prepared MNPs were washed with a mixture of ethanol and double-deionized water, then subjected to centrifugation at 2000 rpm for 20 min. The resultant precipitate obtained from the experiments underwent drying in a vacuum oven and was eventually pulverized into a powder. The procedure was extended for the development of DEuFO MNPs and in this instance, dextran was dispersed directly in double-deionized water instead of a 0.1 M acetic acid solution.

Characterization

The phase purity and crystallographic details of the designed magnetic nanoparticles were analysed using X-ray diffraction (Rigaku Ultima IV), and the XRD findings were directed with Cu-K α radiation ($\lambda = 1.5406 \text{ \AA}$). The functional groups and elemental states were studied using Fourier transform infrared spectra (FTIR) analysis accomplished on an Agilent Technology Cary 630 instrument. The morphology and average particle size were

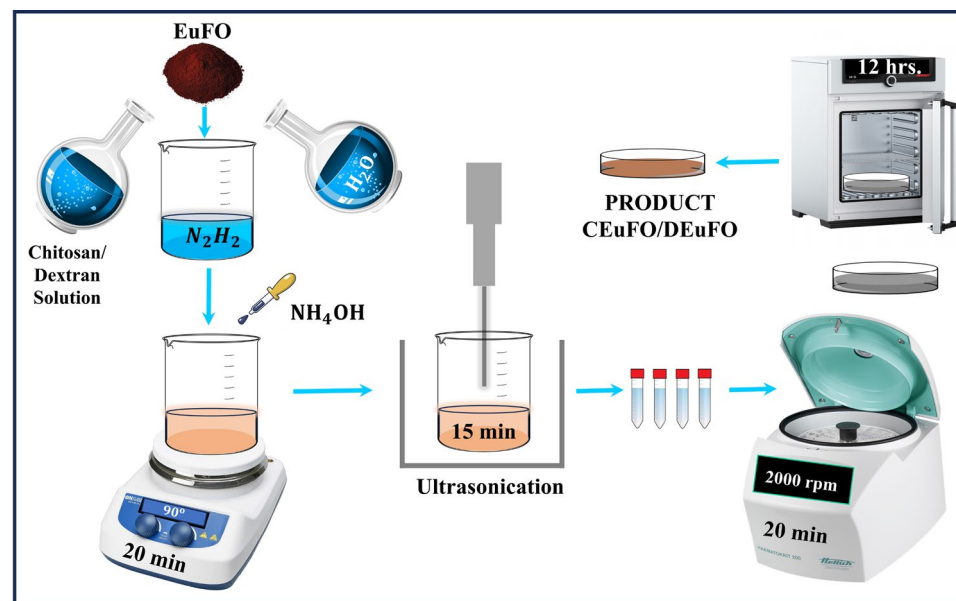


Figure 1. Schematic representation of the synthesized MNPs.

premeditated via ZEISS Gemini 300 field-emission scanning electron microscope (FESEM), while the selected area electron diffraction (SAED) and d-spacing measurements were investigated with JEOL, JEM 2100 high-resolution transmission electron microscope (TEM). The electronic and chemical states of the MNPs were widely observed using X-ray photoelectron spectroscopy on a Thermo Fisher Scientific Excalab Xi + instrument. X-ray radiation from an Al K α source was employed for the analysis. The magnetic parameters of the nanoparticles were examined by a Lakeshore 7410 series vibrating sample magnetometer (VSM) and Electron Spin Resonance (ESR; JEOL, JES-FA200) techniques. The processed MNPs underwent a self-heating study via induction heating setup (Easy Heat-8310, Ambrell make, U.K.).

Results and discussion

Structure and morphology study

The XRD spectra of engineered dextran and chitosan-functionalized Eu doped FO MNPs, as displayed in Fig. 2, portray a pure crystalline phase, which exhibits distinct diffraction peaks ascertained as (220), (311), (400), (511), and (440). Herein, the observed peaks in the X-ray diffraction pattern can be attributed to the cubic spinel structure of Fe_3O_4 , which aligns with the data documented in the ICDD PDF card number 01-075-0033 with space group $Fd\bar{3}m$ ¹⁹. Furthermore, due to the non-crystalline structure of dextran and chitosan, the final product matrix (DEuFO/CEuFO) indicates no alteration of the crystal structure²⁰. Figure 2b gives a precise schematic representation of Eu doped ferrite (generated from VESTA software), which resembles that Eu ions choose to be in the B sites rather than A sites.

The computed structure parameters are enclosed in Table 1, where crystallite size was measured by using the Scherrer formula²⁶. Remarkably, the increasing trend of crystallite size and cell volume indicate the influence of chitosan and dextran. Moreover, the rising trend in crystallite size aligns with the support of TEM analysis. The polymers may affect nucleation and growth processes, leading to larger crystallites. The observed changes in the crystal structure attributed to developed lattice strain⁴, stress, cation re-arrangement, and finite size effect²⁷ can be attributed to the active involvement of chitosan and dextran, which bring about structural modifications at

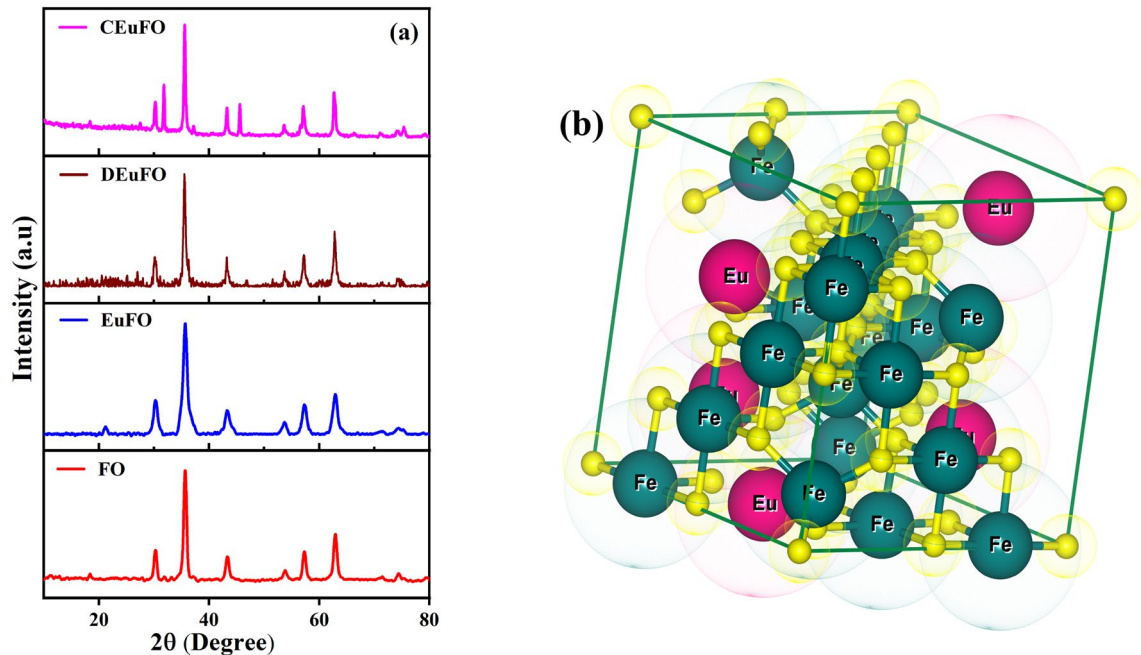


Figure 2. (a) XRD; Rietveld refinement of the reference MNPs (b) Ball-and-stick model of *fcc* cubic spinel structure of EuFO MNPs.

Sample name	FO	EuFO	CEuFO	DEuFO
Crystallite size (nm)	14.21	15.57	16.71	16.79
Particle size D _{TEM} (nm)	14 ± 3	15 ± 3	17 ± 2	17 ± 3
ε	0.004	0.005	0.006	0.005
Cell volume (Å)	581.65	582.29	582.50	582.52
U+12E8 _D (× 10 ⁻²)	0.39	0.38	0.38	0.36

Table 1. Crystallite size, particle size, strain (ε), cell volume, and dislocation density (U+12E8_D).

the atomic and molecular levels. To counter this effect, the variation in dislocation density with the encapsulation of chitosan and dextran highlights the influence of the densification progression, which is sensible due to the physical characteristics of cations, their valence states, and distribution on A and B sites.

Figure 3 illustrates the FTIR spectra of the engineered MNPs, under the frequency limit 400–4000 cm⁻¹. In this regard, a broad absorption band of approximately ~ 3450 to 3550 cm⁻¹ was observed, corresponding to the stretching vibrations of O-H bonds in the absorbed H₂O molecule, and this observation aligns with the documented previous literature³¹. To continue with this, the presence of two extra absorption peaks at approximately 1595 cm⁻¹ and 1371 cm⁻¹ suggests the signature of N-H bending and C-O stretching, strongly signifying the successful functionalization of chitosan on the surface of the processed CEuFO MNPs^{30,31}. Consequently, the DTbFO spectra exhibit an extra peak in the limit of nearly 1000–1250 cm⁻¹, which can be ascribed to the signature C-O and C-O-C stretching of the polymeric chain of dextran, indicating the effective encapsulation of dextran in the respective EuFO system⁸. However, the processed MNPs display distinct absorption peaks at approximately 428 and 540 cm⁻¹ in their spectrum, indicating signature traits of the spinel ferrite structure³³. More in detail, the absorption peaks at around 540 cm⁻¹ (ν_1) and 428 cm⁻¹ (ν_2) are a result of the stretching vibration of the Fe-O bonds in the tetrahedral (A) and octahedral (B) metal complexes, respectively³⁴. Furthermore, Fig. 3 demonstrates the shift of the absorption band (ν_2) towards higher wavenumbers at approximately 428 cm⁻¹ due to the presence of Europium ions in the octahedral sites of the FO matrix, which aligns with the findings obtained from the computed XRD analysis.

The surface morphology of the reference MNPs is studied via SEM analysis, where Fig. 4a portrays the chitosan-coated Eu-doped FO MNPs. The SEM micrograph of CEuFO MNPs shows a nearly uniform, berry-like

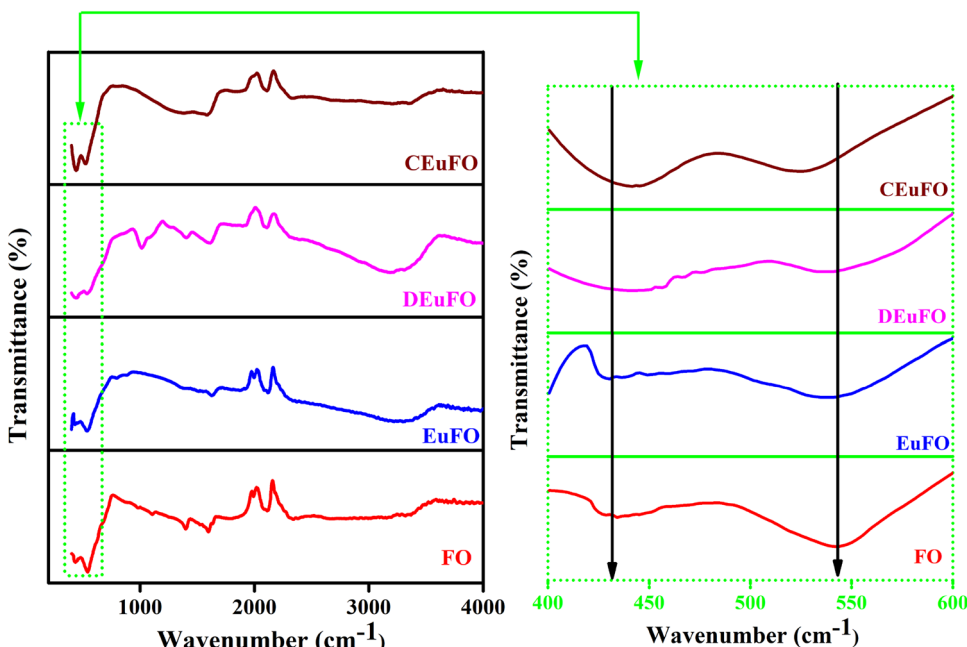


Figure 3. FTIR spectra of the synthesized MNPs.

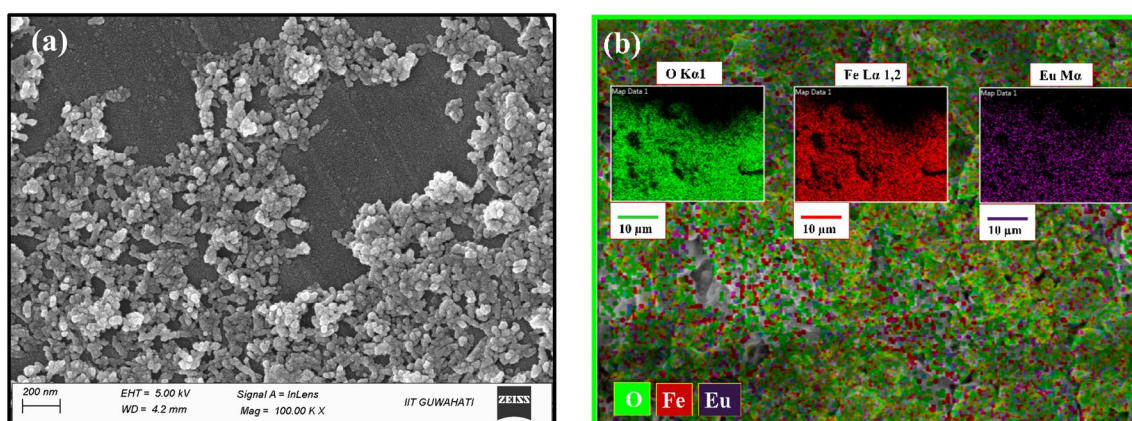


Figure 4. (a) SEM image of CEuFO MNPs (b) Elemental mapping of EuFO MNPs.

structure. In addition, elemental mapping from SEM images (EuFO MNPs) conveys the existence of the elements Fe, O, and Eu, respectively, as depicted in Fig. 4b.

The TEM images of the reference MNPs are portrayed in Fig. 5. The effective addressing of excellent dispersion is demonstrated through the TEM images, indicating that the designed synthesis approach efficiently prevents agglomeration issues. These findings are in excellent agreement with the observations obtained from SEM analysis. Additionally, the d-spacing values consistent with the (311) plane of the characterized EuFO, CEuFO, and DEuFO MNPs match perfectly with the calculated XRD data (Fig. 5b,d,f). The particle size is calculated through the lognormal distribution (Fig. 5h), and the estimation method is strongly aligned with the XRD findings, as depicted in Table 1. The increment in particle size can be accredited to the co-existence of polymers (chitosan/dextran) and dopants (Eu), resulting in particle size and shape modification. The difference in nanoparticle size between chitosan and dextran coatings could be attributed to charges from chitosan macromolecules, which are absent in dextran-coated MNPs. Conversely, the positively charged amino groups in chitosan-coated MNPs create electrostatic repulsion among the CEuFO, preventing their aggregation and forming smaller, isolated particles¹⁷. In this regard, the absence of charges (amino group) in dextran can contribute to partial agglomeration of the MNPs, foremost to an increase in particle sizes. The presence of concentric circles with bright spots in the SAED pattern is depicted in Fig. 5g, signifying that the MNPs are polycrystalline in nature³⁵. The spotty rings observed in the SAED pattern are consistent with the Bragg planes and align well with the results obtained from XRD analysis.

The effective doping and coating of the processed MNPs can be investigated via XPS analysis as enclosed in Fig. 6. The overall survey scans of DEuFO MNPs are displayed in Fig. 6a, implying the successful functionalization of dextran (composed of hydroxyl group) and proper doping of rare-earth element (Eu) in the FO matrix. Following the scan results in Fig. 6b, the satellite Fe peaks examined in the scan correspond to the formation of bonds initiated by both octahedral (O_h) and tetrahedral sites (T_h), exhibiting valence states of +2 and +3. The high-resolution core Fe 2p electron spectra of DEuFO MNPs show distinct peaks at approximately ~711 eV and ~722 eV, corresponding to the spin-orbital properties of $2p_{3/2}$ and $2p_{1/2}$, respectively³⁶. The satellite peak of the C 1 s scan in Fig. 6c provides a deep insight into the existence of dextran in the system. The deconvolution of Eu $4d_{5/2}$ and Eu $4d_{3/2}$, revealing approximate binding energies of around ~136 eV and ~143 eV (Fig. 6d), indicates the presence of two bonds initiating from the Eu ions.

Magnetic analysis

The magnetic characteristics and spin-related phenomena of the magnetic nanoparticles (MNPs) were assessed using ESR spectroscopy, as depicted in Fig. 7. The observed broadening in the ESR spectra reveals a Lande g factor near to ~2, providing evidence for the presence of a superparamagnetic phase in the synthesized magnetic nanoparticles (MNPs)³⁷. In particular, the observed broadening of the curves signifies the predominance of dipolar interactions³⁸. The results obtained from the ESR findings are presented in Table 2, encompassing essential characteristics such as spin–spin relaxation time (τ_1), spin–lattice relaxation time (τ_2), resonance field (H_r), resonance linewidth (H_{pp}), effective g value, and full width at half maximum (FWHM) of the absorption spectra ($\Delta H_{1/2} = \sqrt{3} H_{pp}$)³⁹. Herein, the diminished magnitudes of both g and H_{pp} values indicate the substantial influence of potent super-exchange interactions. Subsequently, the reduced g and H_{pp} values observed in the case of dextran and chitosan-coated MNPs in comparison to bare and Eu-doped MNPs exemplify a random orientation of magnetic moments, concurrent with the VSM study⁴¹.

Moreover, within the context of the magnetic fluid hyperthermia (MFH) investigation, the SAR emerges as a basic threshold for quantifying the self-heating efficacy of the magnetic assembly, and it relates inversely to the relaxation time. As enclosed in Table 2, the recorded decrease in spin–spin relaxation time (τ_1) for the coated MNPs compared to the uncoated counterpart signifies a higher SAR, further confirmed by induction heating analysis³⁹.

The magnetic parameters of the synthesized MNPs are represented in Fig. 8. The S-shaped hysteresis graphs were subjected to analysis using the Langevin fit, unveiling the nearly superparamagnetic behavior of the nanoparticles⁴³.

For precise assessment of saturation magnetization (M_s) and effective anisotropy constant (K_{eff}), employing the Law of Approach to Saturation Magnetization (LAS) to fit the S-shaped graphs⁴⁴. The attained magnetic characteristics, comprising saturation magnetization (M_s), effective anisotropy constant (K_{eff}), retentivity (M_r), and coercivity (H_c), are enclosed in Table 3.

As evidenced by the magnetic findings presented in Table 3, it is observed that the M_s of the EuFO MNPs parades a significant decrease compared to the pure FO MNPs. The reduction in M_s observed here is primarily attributed to the impact of size effect and spin randomness induced through spin canting at the surfaces⁴⁵, which signify a direct concurrence between the magnetic and structural states of the examined MNPs⁴⁶. As revealed by XRD analysis, the substitution of Eu³⁺ cations into the octahedral Fe³⁺ sites leads to elongation in bond lengths $Fe^{3+}(Eu^{3+})-O^{2-}$, and as the bond lengths elongate, the coordination of cations weakens, resulting in a more pronounced oxygen deficiency; notably, this reduces exchange interaction and magnetic parameters⁴⁷. Albeit, the reduction in M_s observed in coated MNPs can primarily be ascribed to surface-induced spin canting, magnetic dilution from the non-magnetic characteristics of chitosan and dextran coatings, along with interfacial effects and collective oscillations⁴⁸. Additionally, the presence of a coating on the samples inhibits aggregation that arises due to dipolar interactions among magnetic cores, consequently enhancing the colloidal stability. This characteristic also brings the advantage of restraining the interaction between Fe²⁺ ions and enzymes, subsequently lowering the promotion of reactive oxygen species generation through the Fenton reaction⁵⁰. Besides, the Rietveld refinement further corroborates the reconfiguration of cation distribution within the CEuFO and DEuFO MNPs. The observed increase in the M_s of DEuFO comparison to CEuFO can be accredited to the ligand characteristics of

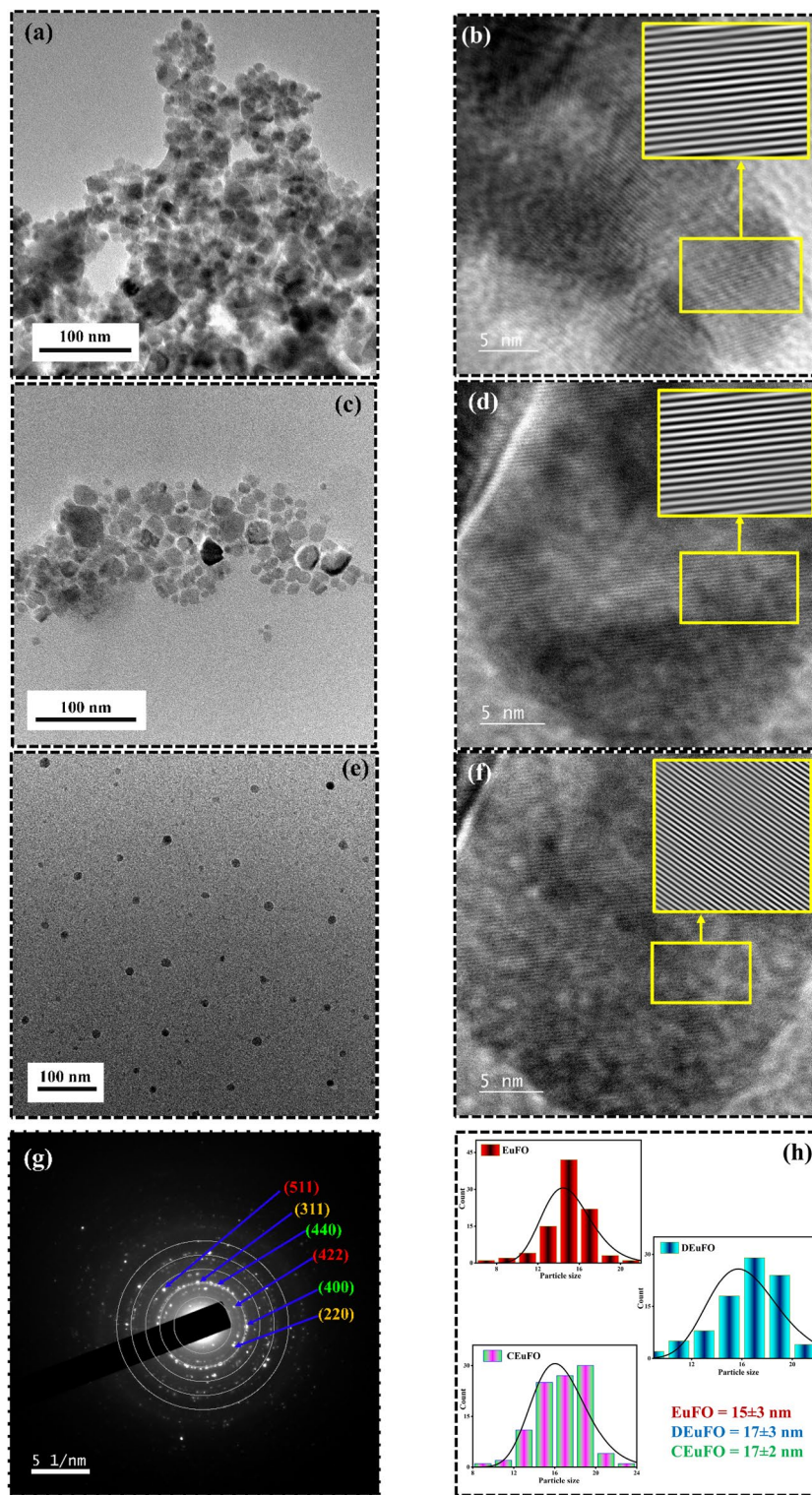


Figure 5. TEM images: (a) EuFO MNPs (b) d-spacing of EuFO MNPs (c) DEuFO MNPs (d) d-spacing of DEuFO MNPs (e) CEuFO MNPs (f) d-spacing of CEuFO MNPs (g) SAED inset of DEuFO MNPs (h) lognormal distribution for all the reference MNPs.

chitosan and dextran, where ligands act to influence the crystal field splitting following the principles of ligand field theory^{51,52}. The findings suggest that dextran-coated MNPs prefer a high spin state of Fe^{3+} within the octahedral site, owing to the presence of a hydroxyl group serving as a weak field ligand⁵³. Conversely, chitosan-coated

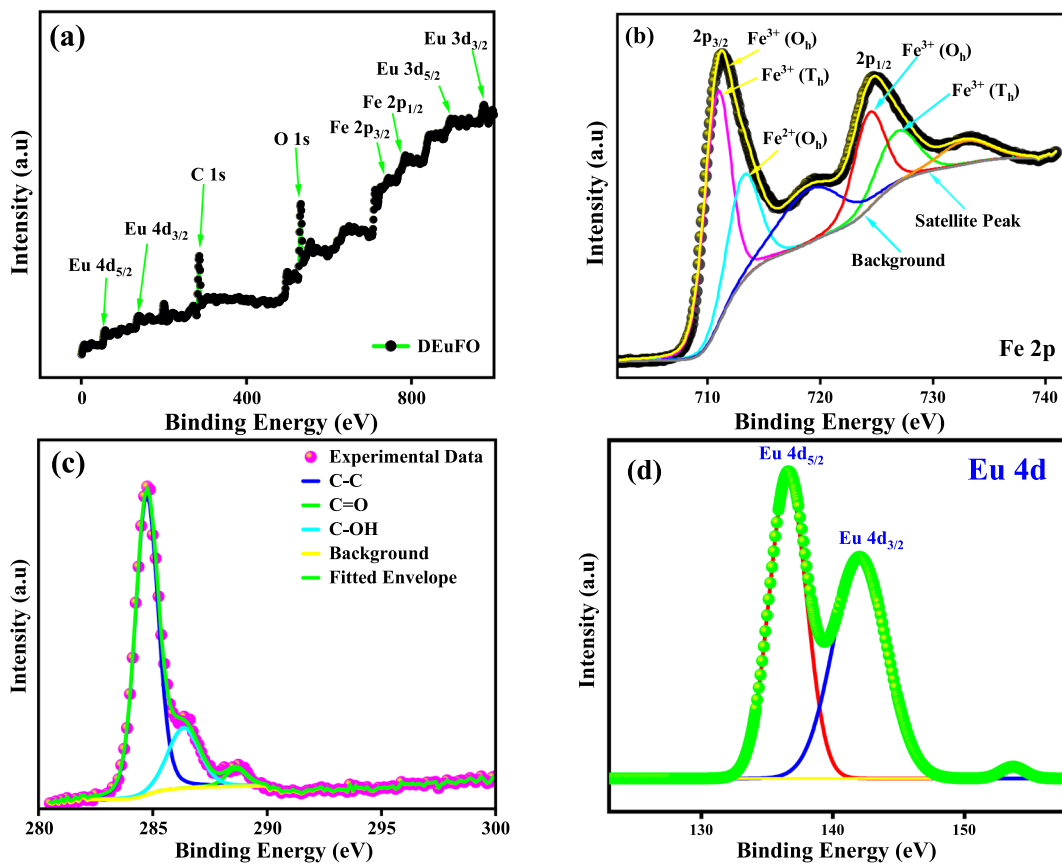


Figure 6. XPS scans of DEuFO; (a) complete survey of DEuFO MNPs (b) Fe 2p spectra (c) C 1 s spectra (d) Eu 4d spectra.

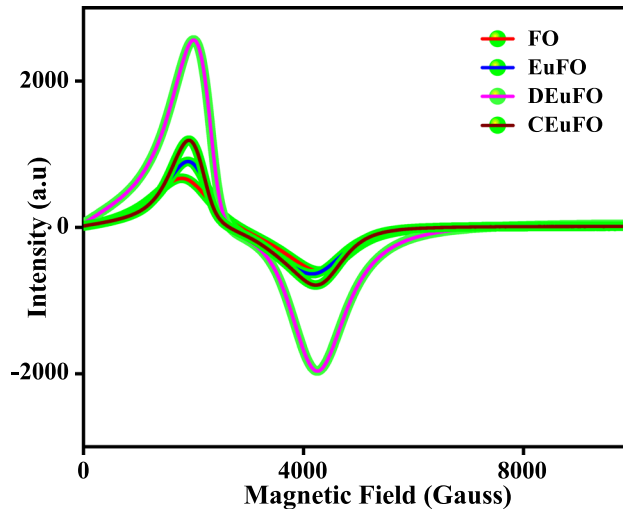


Figure 7. ESR spectra of the reference MNPs.

MNPs display a greater preference for the low spin state of Fe^{3+} within the octahedral site, primarily attributed to the prevalence of the amine group in chitosan⁵¹. According to the linear response theory, magnetic anisotropy plays a vital role in controlling the heating efficiency of the nanoparticles⁵⁴. In this regard, diverse approaches on the topic, the impact of effective anisotropy⁵⁵ on the SAR of suitably designed MNP systems remains a subject of ongoing controversy. Moreover, theoretically Fu et al.⁵⁶ and experimentally Serantes et al.⁵⁷ highlighted that these chain-like structures positively impact the magnetic anisotropy and lead to the enhancement of the heating efficiency. Luis et al. investigated the nanoparticle heating efficiency and reported that the heating efficiency

Sample details	$\tau_1 \times 10^{-11}$ (sec)	$\tau_2 \times 10^{-12}$ (sec)	g	H_{pp} (Gauss)	$\Delta H_{1/2}$ (Gauss)	H_r (Gauss)
FO	6.85	1.03	2.02	2530	4382	2835
EuFO	7.51	0.94	2.02	2219	3843	2728
DEuFO	7.30	0.97	2.02	2218	3841	2652
CEuFO	7.27	0.98	2.02	2217	3839	2640

Table 2. Measured ESR parameter (spin–spin relaxation time τ_1 , spin–lattice relaxation time τ_2 , effective g value, resonance linewidth H_{pp} , FWHM of the absorption spectra $\Delta H_{1/2}$, and resonance field H_r).

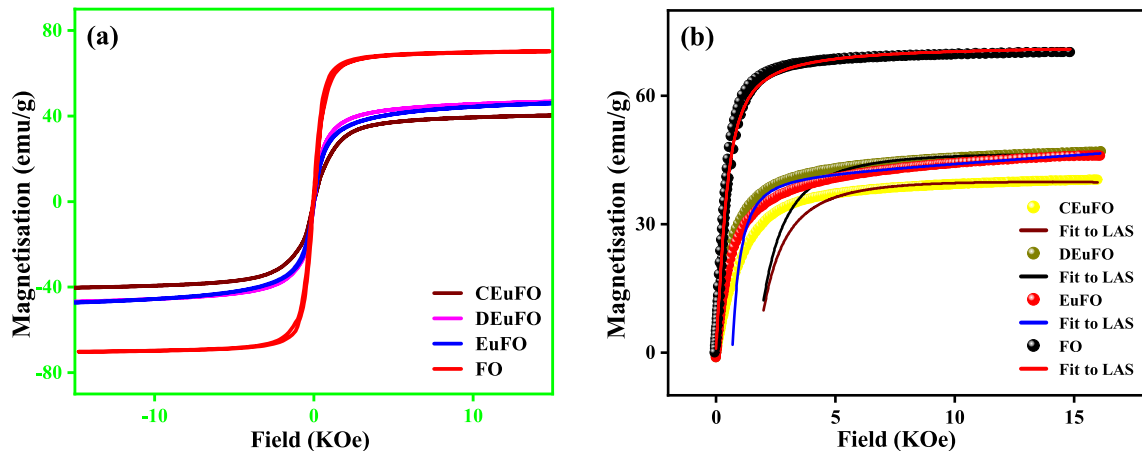


Figure 8. (a) M–H hysteresis loop for the reference MNPs (b) LAS fit of the reference MNPs.

Sample details	M_s (emu/g)	H_c (Oe)	M_r (emu/g)	$k_{eff} \times 10^5$ (erg/cm ³)
FO	70.61	22	2.59	2.56
EuFO	46.26	9	1.21	2.26
DEuFO	46.02	6	0.82	1.79
CEuFO	40.89	4	0.76	2.58

Table 3. Magnetic parameters: Saturation magnetization (M_s), Coercivity (H_c), Retentivity (M_r), and effective anisotropy constant (K_{eff}).

has profoundly amplified with low anisotropy⁵⁸. Consistent with the literature, particularly in the magnetic assessment detailed in Table 3 highlights a reduction of effective magnetic anisotropy (K_{eff}) within the dextran and chitosan-coated MNPs compared to the uncoated FO and EuFO MNPs. In this context, the decrease in effective magnetic anisotropy (K_{eff}) observed in DEuFO and CEuFO MNPs can be linked to a weakened interaction between Eu and Fe, resulting in a lowered ratio of spin orbital moments of 4f. electrons and subsequent diminution of the spin–orbit couplings⁵⁹. In addition, from the Stoner–Wohlfarth model⁶⁰, it is evident that the reducing trend in coercivity observed in the reference nanoparticles results from a direct correlation with the reduced value of the effective anisotropy constant⁶⁰.

Self-heating efficiency study

The magnetic heating efficiency of the reference MNPs for magnetic hyperthermia applications is expected to be triggered by an AC magnetic field at a frequency of 337 kHz, with an amplitude of 249 A and a magnetic field strength of 14.92 kAm⁻¹, under the maintenance of clinical safety thresholds ($H_f \leq 5 \times 10^9$ Am⁻¹ s⁻¹)⁶¹. Figure 9 illustrates the time-dependent temperature profile at a concentration of 1 mg/mL, wherein the Box–Lucas model⁶² was applied to determine the specific absorption rates (SAR) and intrinsic loss power (ILP) of the reference MNPs. In particular, maintaining the hyperthermic range and enhancing the SAR depends on the presence of optimal concentrations of nanoparticles. Theoretically, an optimal concentration for achieving maximum SAR was initially proposed by Haase et al.⁶³, and experimentally confirmed by Lahiri et al.⁶⁴. Similarly, Tan et al. elucidated the significant influence of optimal concentration on the heating power dissipation using Monte Carlo simulations⁶⁵. Based on these prior investigations, optimized the concentration to 1 mg/mL, and the graph (Fig. 9) illustrates that all the synthesized nanoparticles are evident in the hyperthermic threshold range (42 °C to 47 °C)⁶⁶. Only a limited number of studies have precisely grasped the influence of particle size distribution on

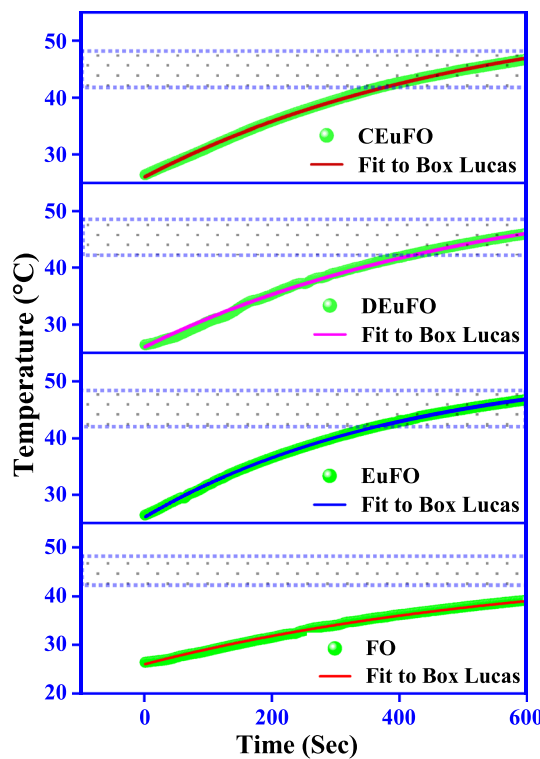


Figure 9. Box-Lucas fit of time-dependent temperature deviation curve for synthesized MNPs for 1 mg/mL concentrations.

the heating efficiency of MNPs. In this regard, an essential remark was found by Zubarev et al. that the intrinsic interaction of MNPs with diameters of 17–20 nm can significantly lead to up to 30% higher heat production⁶⁷.

In practical scenarios, modifying essential parameters that control magnetic hyperthermia performance, like adjusting the viscosity in particular biological systems or addressing the limitations of nanoparticle rotation within cells or tissues, is challenging^{68,69}. Hence, to amplify hyperthermia performance, it is essential to optimize Néel relaxation parameters, which remain unaltered by the biological microenvironment, given the negligible contribution of Brownian relaxation⁷⁰. Analogously, Fig. 10 depicts the variation of SAR and ILP of the reference nanoparticles, and it is observed that even though the magnetic parameters (M_s and K_{eff}) of DEuFO and CEuFO MNPs are lowered, they exhibit improved heating efficiency compared to the uncoated nanoparticles. Nevertheless, the challenge of simultaneously optimizing all parameters under diverse experimental conditions for magnetic hyperthermia remains unresolved. Therefore, it can be noted that another essential parameter is dipolar interaction and it happens to be dominant among all other inter-particle interactions¹. The dipolar interaction energy in magnetic nanoparticles is directly proportional to $1/r^6$, (r is the inter-particle distance between the particles) indicating that the interaction intensifies as the inter-particle distance decreases. The impact of dipolar

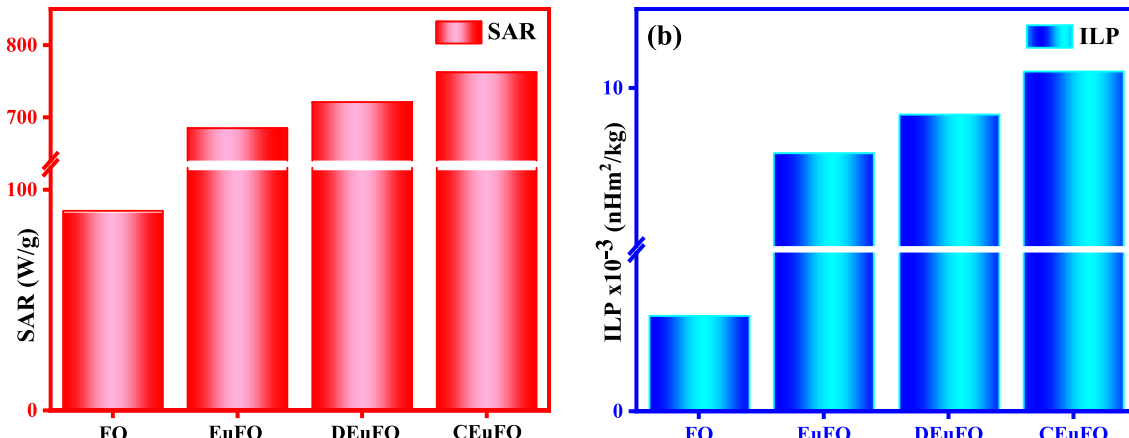


Figure 10. (a) SAR Variation (b) ILP Variation of the reference MNPs.

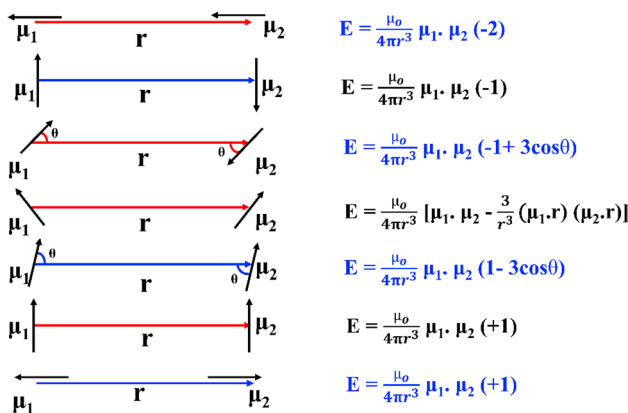


Figure 11. Different alignments for the pair of magnetic dipoles.

interaction on the magnetic relaxations of MNPs, influencing heating efficiency, is subject to debate due to both increasing and decreasing dipolar interactions for self-heating efficiency. To understand the behavior of dipolar interaction-dependent specific absorption rate, Raja Das et al. studied two Fe_3O_4 systems as nanospheres and nanocubes⁷¹. Their results concluded that the weaker intraparticle interactions are preferred as heating mediators. To counter this consequence on MFH performance, Landi et al. reported that dipolar interactions serve to elevate the energy barrier, thereby enhancing the SAR for the magnetically soft particles⁷². Henceforward, the literature reviewed above collectively suggests that the question of achieving optimal heating efficiency remains uncertain, with the roles of magnetocrystalline anisotropy and dipolar interaction. By considering theoretical and experimental findings on heat dissipation via relaxation mechanisms, Dормann-Bessais-Fiorani proposes a modified model for Neel relaxation [$\tau_N = \tau_0 \exp(\frac{\Delta E^*}{KT})$] in the presence of other energy terms⁷³, where $\Delta E^* = E_A + E_H + E_D$; E_A is the anisotropy barrier, E_H is the Zeeman energy, and E_D is the dipolar interaction energy. As a consequence, it is more convenient to picture the effect of dipolar interaction energy (E_D) to analyze the improvement of heat dissipation of the surface encapsulated nanoparticles (although the effects of E_H can be negligible as followed by the Hergt-Dutz limit⁷⁴). The assumption is justified considering the dipolar energy formula⁷⁵, $E_D = \alpha \mu^2 / d_{ij}^3$, where α is a constant, μ represents the magnetic strength of the MNPs, and d is the separation between two particles i and j . Therefore, E_D imparts a disordering torque, disarranging the spin relaxation mechanism owing to the competition between intraparticle interactions and anisotropy among the nanoparticles⁷⁶. This competition leads to frustrated magnetic moments or disordered easy anisotropy axis orientations, resulting in a demagnetizing effect within the system⁷⁷. This effect could possibly lead to decreased heating efficiency in uncoated MNPs. Another noteworthy finding from Fig. 10 is that the heating response is more pronounced in the CEuFO case than in the DEuFO system. As evident from the TEM analysis, CEuFO MNPs exhibit greater dispersion than DEuFO MNPs, leading to reduced dipolar interaction energy that enhances the SAR. Furthermore, Fig. 11 depicts a range of alignments for a pair of magnetic dipoles, ordered from the lowest to the highest dipole energy configurations. In the initial strategy presented in Fig. 11, the dipole moments are aligned along the vector r in a linear chain configuration, all possessing the same polarity. This arrangement represents the most stable orientation. The tendency to form such chains has significant implications for clustering MNPs and their efficiency in heat generation. Conversely, an antiparallel alignment becomes the most favorable when the dipole moments are oriented perpendicular to the vector r . In our study, mutual dipole interactions can be successfully controlled via appropriate coating of dextran and chitosan, which tends to increase the separation between the magnetic dipoles, which further improved the self-heating efficiency. Based on this, the chitosan-coated Eu-doped Fe_3O_4 MNPs portray a rising heating efficiency among all the fabricated samples, rendering them a safe and efficient agent for hyperthermia applications.

Conclusion

In summary, this study outlines a method for designing Eu-doped FO nanoparticles functionalized with chitosan and dextran, representing how biopolymer encapsulation offers a promising approach to control agglomeration of the reference MNPs. The investigation delves into the impact of controlling dipolar interactions through the relaxation mechanism. The inclusion of chitosan and dextran in the EuFO MNPs contributes to precise structural control and fine-tuned magnetic properties, further enhancing the self-heating efficiency of the characterized MNPs. In particular, the results indicate that the reported SAR value of 762.21 W/g for CEuFO MNPs, which is under safety limit, could open avenues for future investigations to explore the potential use of these MNPs *in vivo* and optimize clinical parameters, prefiguring an intriguing new path toward successful MFH applications.

Data availability

The data that support the findings of this study are available within the article.

Received: 10 January 2024; Accepted: 18 April 2024

Published online: 29 April 2024

References

1. Valdés, D. P., Lima, E., Zysler, R. D., Goya, G. F. & De Biasi, E. Role of anisotropy, frequency, and interactions in magnetic hyperthermia applications: Noninteracting nanoparticles and linear chain arrangements. *Phys. Rev. Appl.* **15**, 1–18 (2021).
2. Pan, J., Xu, Y., Wu, Q., Hu, P. & Shi, J. Mild Magnetic hyperthermia-activated innate immunity for liver cancer therapy. *J. Am. Chem. Soc.* **143**, 8116–8128 (2021).
3. Rajan, A., Sharma, M. & Sahu, N. K. Assessing magnetic and inductive thermal properties of various surfactants functionalised Fe_3O_4 nanoparticles for hyperthermia. *Sci. Rep.* **10**, 1–15 (2020).
4. Hazarika, K. P. & Borah, J. P. RSC Advances parameter tuning, and self heating in magnetic nanoparticles. *RSC Adv.* **13**, 5045–5057 (2023).
5. Xiang, H. *et al.* One-pot synthesis of water-soluble and biocompatible superparamagnetic gadolinium-doped iron oxide nano-clusters. *J. Mater. Chem. B* **8**, 1432–1444 (2020).
6. Fu, R., Yan, Y., Roberts, C., Liu, Z. & Chen, Y. The role of dipole interactions in hyperthermia heating colloidal clusters of densely-packed superparamagnetic nanoparticles. *Sci. Rep.* **8**, 1–10 (2018).
7. Kurihara, Y., Yokota, H. & Takahashi, M. Water-dispersible carboxymethyl dextran-coated melamine nanoparticles for biosensing applications. *ACS omega* **7**(45), 41641–41650 (2022).
8. Naha, P. C. *et al.* Dextran-coated cerium oxide nanoparticles: A computed tomography contrast agent for imaging the gastrointestinal tract and inflammatory bowel disease. *ACS Nano* **14**, 10187–10197 (2020).
9. Sugumaran, P. J., Liu, X. L., Herring, T. S., Peng, E. & Ding, J. GO-functionalized large magnetic iron oxide nanoparticles with enhanced colloidal stability and hyperthermia performance. *ACS Appl. Mater. Interfaces* **11**, 22703–22713 (2019).
10. Lima, E., Brandl, A. L., Arelaro, A. D. & Goya, G. F. Spin disorder and magnetic anisotropy in Fe_3O_4 nanoparticles. *J. Appl. Phys.* **99**, 083906 (2006).
11. Linh, P. H. *et al.* Dextran coated magnetite high susceptibility nanoparticles for hyperthermia applications. *J. Magn. Magn. Mater.* **460**, 128–136 (2018).
12. Naha, P. C. *et al.* Dextran-coated iron oxide nanoparticles as biomimetic catalysts for localized and pH-activated biofilm disruption. *ACS Nano* **13**, 4960–4971 (2019).
13. Mdlalose, W. B., Mokhosi, S. R., Dlamini, S., Moyo, T. & Singh, M. Effect of chitosan coating on the structural and magnetic properties of MnFe_2O_4 and $\text{Mn}_{0.5}\text{Co}_{0.5}\text{Fe}_2\text{O}_4$ nanoparticles. *AIP Adv.* **8**, 6 (2018).
14. Bae, K. H. *et al.* Chitosan oligosaccharide-stabilized ferrimagnetic iron oxide nanocubes for magnetically modulated cancer hyperthermia. *ACS Nano* **6**, 5266–5273 (2012).
15. Oh, Y., Lee, N., Kang, H. W. & Oh, J. In vitro study on apoptotic cell death by effective magnetic hyperthermia with chitosan-coated MnFe_2O_4 . *Nanotechnology* **27**, 115101 (2016).
16. Shakil, M. S. *et al.* In vivo toxicity studies of chitosan-coated cobalt ferrite nanocomplex for its application as MRI contrast dye. *Appl. Bio Mater.* **3**, 7952–7964 (2020).
17. Aranaz, I. *et al.* Chitosan: An overview of its properties and applications. *Polymers* **13**(19), 3256 (2021).
18. Hazarika, K. P. & Borah, J. P. A comprehensive scrutiny to controlled dipolar interactions to intensify the self-heating efficiency of biopolymer encapsulated Tb doped magnetite nanoparticles. *Sci. Rep.* **14**, 1–15 (2024).
19. Shattoot, S., Mozaffari, M., Reiter, G., Zahn, D. & Dutz, S. Heat dissipation in Sm^{3+} and Zn^{2+} co-substituted magnetite ($\text{Zn}_{0.1}\text{Sm}_x\text{Fe}_{2.9-x}\text{O}_4$) nanoparticles coated with citric acid and pluronic F127 for hyperthermia application. *Sci. Rep.* **11**, 16795 (2021).
20. Pourmortazavi, S. M., Sahebi, H., Zandavar, H. & Mirsadeghi, S. Fabrication of Fe_3O_4 nanoparticles coated by extracted shrimp peels chitosan as sustainable adsorbents for removal of chromium contaminates from wastewater: The design of experiment. *Compos. Part B Eng.* **175**, 107130 (2019).
21. Phan, M. H. *et al.* Exchange bias effects in iron oxide-based nanoparticle systems. *Nanomaterials* **6**, 221 (2016).
22. Praveena, K. *et al.* Crystallographic, magnetic and electrical properties of $\text{Ni}_{0.5}\text{Cu}_{0.25}\text{Zn}_{0.25}\text{La}_{x}\text{Fe}_{2-x}\text{O}_4$ nanoparticles fabricated by sol-gel method. *J. Magn. Magn. Mater.* **321**, 213–220 (2014).
23. Zeng, X. *et al.* Direct imaging of dopant sites in rare-earth element-doped permanent magnet and correlated magnetism origin. *Nanoscale* **11**, 4385–4393 (2019).
24. Antic, B., Kremenovic, A., Nikolic, A. S. & Stoiljkovic, M. Cation distribution and size-strain microstructure analysis in ultrafine Zn-Mn ferrites obtained from acetylacetone complexes. *J. Phys. Chem. B* **108**, 12646–12651 (2004).
25. Rodríguez-Carvajal, J. & Roisnel, T. January. Line broadening analysis using FullProf*: Determination of microstructural properties. *Mater. Sci. Forum* **443**, 123–126 (2004).
26. Gul, I. H., Abbasi, A. Z., Amin, F., Anis-ur-Rehman, M. & Maqsood, A. Structural, magnetic and electrical properties of $\text{Co}_{1-x}\text{Zn}_x\text{Fe}_2\text{O}_4$ synthesized by co-precipitation method. *J. Magn. Magn. Mater.* **311**, 494–499 (2007).
27. Paswan, S. K. *et al.* Optimization of structure-property relationships in nickel ferrite nanoparticles annealed at different temperature. *J. Phys. Chem. Solids* **151**, 109928 (2021).
28. Aman, S. *et al.* Synthesis and characterization of copper-based spinel ferrites for high frequency applications. *J. Magn. Magn. Mater.* **547**, 168778 (2022).
29. Thakur, P. *et al.* Gd^{3+} doped Mn-Zn soft ferrite nanoparticles: Superparamagnetism and its correlation with other physical properties. *J. Magn. Magn. Mater.* **432**, 208–217 (2017).
30. Jagadeesha Angadi, V. *et al.* Magnetic properties of larger ionic radii samarium and gadalonium doped manganese zinc ferrite nanoparticles prepared by solution combustion method. *J. Magn. Magn. Mater.* **529**, 167899 (2021).
31. Nam, P. H. *et al.* Physical characterization and heating efficacy of chitosan-coated cobalt ferrite nanoparticles for hyperthermia application. *E Phys. E Low-Dimens. Syst. Nanostruct.* **134**, 114862 (2021).
32. Lachowicz, D. *et al.* Enhanced hyperthermic properties of biocompatible zinc ferrite nanoparticles with a charged polysaccharide coating. *J. Mater. Chem. B* **7**, 2962–2973 (2019).
33. Hazarika, K. P. & Borah, J. P. Biocompatible Tb doped Fe_3O_4 nanoparticles with enhanced heating efficiency for magnetic hyperthermia application. *J. Magn. Magn. Mater.* **560**, 251–256 (2022).
34. Patange, S. M. *et al.* Elastic properties of nanocrystalline aluminum substituted nickel ferrites prepared by co-precipitation method. *J. Mol. Struct.* **1038**, 40–44 (2013).
35. Abbas, Y. M., Mansour, A. B., Ali, S. E. & Ibrahim, A. H. Investigation of structural and magnetic properties of multiferroic $\text{La}_{1-x}\text{Y}_x\text{Fe}_3\text{O}_3$ Perovskites, prepared by citrate auto-combustion technique. *J. Magn. Magn. Mater.* **482**, 66–74 (2019).
36. Priya, K., Fopase, R., Pandey, L. M. & Borah, J. P. Influence of Gd-doping on structural, magnetic, and self-heating properties of Fe_3O_4 nanoparticles towards magnetic hyperthermia applications. *BPhys. B Phys. Condens. Matter* **645**, 414237 (2022).
37. Mukherjee, S., Pal, A. K., Bhattacharya, S. & Chattopadhyay, S. Field-induced spin-flop transitions of interacting nanosized $\alpha\text{-Fe}_2\text{O}_3$ particles dispersed in a silica glass matrix. *J. Phys. Condens. Matter* <https://doi.org/10.1088/0953-8984/20/05/055204> (2008).
38. Das, R., Chaudhuri, U., Chanda, A. & Mahendiran, R. Broadband Electron Spin Resonance Study in a $\text{Sr}_2\text{FeMoO}_6$ Double Perovskite. *ACS Omega* **5**, 17611–17616 (2020).
39. Massoudi, J. *et al.* Magnetic and spectroscopic properties of Ni-Zn-Al ferrite spinel: From the nanoscale to microscale. *RSC Adv.* **10**(34556), 34580 (2020).
40. Shukla, V. K. & Mukhopadhyay, S. Transverse spin relaxation and magnetic correlation in $\text{Pr}_{1-x}\text{Ca}_x\text{MnO}_3$: Influence of particle size variation and chemical doping *arXiv* 1–8 (2017).

41. Vasilchikova, T. *et al.* Peculiarities of magnetic ordering in the S=5/2 two-dimensional square-lattice antimonate NaMnSbO₄. *Phys. Rev. B* **101**, 1–12 (2020).
42. Lado, J. L., Ferrón, A. & Fernández-Rossier, J. Exchange mechanism for electron paramagnetic resonance of individual adatoms. *Phys. Rev. B* **96**, 1–6 (2017).
43. Lemine, O. M., Madkhali, N., Hjiri, M., All, N. A. & Aida, M. S. Comparative heating efficiency of hematite (α -Fe₂O₃) and nickel ferrite nanoparticles for magnetic hyperthermia application. *Ceram. Int.* **46**, 28821–28827 (2020).
44. Gholizadeh, A. A comparative study of the physical properties of Cu-Zn ferrites annealed under different atmospheres and temperatures: Magnetic enhancement of Cu_{0.5}Zn_{0.5}Fe₂O₄ nanoparticles by a reducing atmosphere. *J. Magn. Magn. Mater.* **452**, 389–397 (2018).
45. Labaye, Y. *et al.* Surface anisotropy in ferromagnetic nanoparticles. *J. Appl. Phys.* **8715**, 1–4 (2002).
46. Li, Q. *et al.* Correlation between particle size/domain structure and magnetic properties of highly crystalline Fe₃O₄ nanoparticles. *Sci. Rep.* **7**, 1–4 (2017).
47. Nasir, M. *et al.* Role of antisite disorder, rare-earth size, and superexchange angle on band gap, curie temperature, and magnetization of R₂NiMnO₆ double perovskites. *ACS Appl. Electron. Mater.* **1**, 141–153 (2019).
48. Myrovali, E. *et al.* Toward the separation of different heating mechanisms in magnetic particle hyperthermia. *ACS Omega* **8**, 12955–12967 (2023).
49. Dhavale, R. P. *et al.* Chitosan coated magnetic nanoparticles as carriers of anticancer drug Telmisartan: pH-responsive controlled drug release and cytotoxicity studies. *J. Phys. Chem. Solids* **148**, 109749 (2021).
50. León Félix, L. *et al.* Gold-decorated magnetic nanoparticles design for hyperthermia applications and as a potential platform for their surface-functionalization. *Sci. Rep.* **9**, 1–11 (2019).
51. Trueba, A., Aramburu, J. A., Barriuso, M. T. & Moreno, M. Spectrochemical series and the dependence of Racah and 10 Dq parameters on the metal-ligand distance: Microscopic origin. *J. Phys. Chem. A* **115**, 1423–1432 (2011).
52. Chakraborty, I. *et al.* Magnetic field-dependent photoluminescence of tartrate-functionalized gadolinium-doped manganese ferrite nanoparticles: A potential therapeutic agent for hyperbilirubinemia treatment. *ACS Appl. Nano Mater.* **4**, 4379–4387 (2021).
53. Tassa, C., Shaw, S. Y. & Weissleder, R. Dextran-coated iron oxide nanoparticles: A versatile platform for targeted molecular imaging, molecular diagnostics, and therapy. *Acc. Chem. Res.* **44**, 842–852 (2011).
54. Rammer, J. (2004). Quantum Transport Theory (1st ed.). CRC Press. <https://doi.org/10.1201/9780429502835>
55. Saville, S. L. *et al.* Journal of Colloid and Interface Science The formation of linear aggregates in magnetic hyperthermia : Implications on specific absorption rate and magnetic anisotropy. *J. Colloid Interface Sci.* **424**, 141–151 (2014).
56. Fu, R., Yan, Y. Y. & Roberts, C. Study of the effect of dipole interactions on hyperthermia heating the cluster composed of superparamagnetic nanoparticles. *AIP Adv.* **5**, 127232 (2015).
57. Serantes, D. *et al.* Multiplying magnetic hyperthermia response by nanoparticle assembling. *J. Phys. Chem. C* **118**, 5927–5934 (2014).
58. Branquinho, L. C. *et al.* Effect of magnetic dipolar interactions on nanoparticle heating efficiency: Implications for cancer hyperthermia. *Sci. Rep.* **3**, 20–22 (2013).
59. Luo, C. *et al.* The influence of Nd dopants on spin and orbital moments in Nd-doped permalloy thin films. *Appl. Phys. Lett.* **105**, 082405 (2014).
60. Kahmann, T., Rösch, E. L., Enpuku, K., Yoshida, T. & Ludwig, F. Determination of the effective anisotropy constant of magnetic nanoparticles: Comparison between two approaches. *J. Magn. Magn. Mater.* **519**, 167402 (2021).
61. Kossatz, S. *et al.* High therapeutic efficiency of magnetic hyperthermia in xenograft models achieved with moderate temperature dosages in the tumor area. *Pharm. Res.* **31**, 3274–3288 (2014).
62. Lanier, O. L. *et al.* Evaluation of magnetic nanoparticles for magnetic fluid hyperthermia. *Int. J. Hyperth.* **36**, 687–701 (2019).
63. Haase, C. & Nowak, U. Role of dipole-dipole interactions for hyperthermia heating of magnetic nanoparticle ensembles. *Phys. Rev. B Condens. Matter Mater. Phys.* **85**, 2–6 (2012).
64. Ranoo, S., Lahiri, B. B., Nandy, M. & Philip, J. Enhanced magnetic heating efficiency at acidic pH for magnetic nanoemulsions stabilized with a weak polyelectrolyte. *J. Colloid Interface Sci.* **579**, 582–597 (2020).
65. Tan, R. P., Carrey, J. & Respaut, M. Magnetic hyperthermia properties of nanoparticles inside lysosomes using kinetic Monte Carlo simulations: Influence of key parameters and dipolar interactions, and evidence for strong spatial variation of heating power. *Phys. Rev. B - Condens. Matter Mater. Phys.* **90**, 1–12 (2014).
66. Rosensweig, R. E. heating magnetic fluid with alternating magnetic field. *J. Urol.* **252**, 370–374 (2002).
67. Zubarev, A. Y. Magnetic hyperthermia in a system of immobilized magnetically interacting particles. *Phys. Rev. E* **99**, 1–6 (2019).
68. Cabrera, D. *et al.* Dynamical magnetic response of iron oxide nanoparticles inside live cells. *ACS Nano* **12**, 2741–2752 (2018).
69. Vargas-Osorio, Z. *et al.* Novel synthetic routes of large-pore magnetic mesoporous nanocomposites (SBA-15/Fe₃O₄) as potential multifunctional theranostic nanodevices. *J. Mater. Chem. B* **5**, 9395–9404 (2017).
70. Soukup, D., Moise, S., Céspedes, E., Dobson, J. & Telling, N. D. In situ measurement of magnetization relaxation of internalized nanoparticles in live cells. *ACS Nano* **9**, 231–240 (2015).
71. Nematici, Z. *et al.* Improving the heating efficiency of iron oxide nanoparticles by tuning their shape and size. *J. Phys. Chem. C* **122**, 2367–2381 (2018).
72. Landi, G. T. Role of dipolar interaction in magnetic hyperthermia. *Phys. Rev. B Condens. Matter Mater. Phys.* **89**, 1–6 (2014).
73. Jacob, N. *et al.* Effects of magnetic dipolar interactions on the specific time constant in superparamagnetic nanoparticle systems. *J. Phys. D. Appl. Phys.* **49**, 295001 (2016).
74. Vassallo, M. *et al.* Improvement of hyperthermia properties of iron oxide nanoparticles by surface coating. *ACS Omega* **8**(2), 2143–2154 (2023).
75. Allia, P. *et al.* Granular Cu-Co alloys as interacting superparamagnets. *Phys. Rev. B Condens. Matter Mater. Phys.* **64**, 1444201–14442012 (2001).
76. Ralandinliu Kahmei, R. D. & Borah, J. P. Clustering of MnFe₂O₄ nanoparticles and the effect of field intensity in the generation of heat for hyperthermia application. *Nanotechnology* **30**, 035706 (2019).
77. Held, G. A., Grinstein, G., Doyle, H., Sun, S. & Murray, C. B. Competing interactions in dispersions of superparamagnetic nanoparticles. *Phys. Rev. B Condens. Matter Mater. Phys.* **64**, 124081–124084 (2001).

Acknowledgements

The authors would like to acknowledge the Central Instrument Facility (CIF), IIT Guwahati for providing all the necessary facilities required for the characterization of the samples.

Author contributions

K.P.H. collected, synthesized, evaluated, and wrote the main manuscript, and J.P.B. conceptualized and supervised the work.

Competing interests

The authors declare no competing interests.

Additional information

Correspondence and requests for materials should be addressed to J.P.B.

Reprints and permissions information is available at www.nature.com/reprints.

Publisher's note Springer Nature remains neutral with regard to jurisdictional claims in published maps and institutional affiliations.



Open Access This article is licensed under a Creative Commons Attribution 4.0 International License, which permits use, sharing, adaptation, distribution and reproduction in any medium or format, as long as you give appropriate credit to the original author(s) and the source, provide a link to the Creative Commons licence, and indicate if changes were made. The images or other third party material in this article are included in the article's Creative Commons licence, unless indicated otherwise in a credit line to the material. If material is not included in the article's Creative Commons licence and your intended use is not permitted by statutory regulation or exceeds the permitted use, you will need to obtain permission directly from the copyright holder. To view a copy of this licence, visit <http://creativecommons.org/licenses/by/4.0/>.

© The Author(s) 2024